INTERNATIONAL JOURNAL FOR NUMERICAL METHODS IN FLUIDS, VOL. 13, 109–129 (1991)

MODELLING THE INITIAL MOTION OF LARGE CYLINDRICAL AND SPHERICAL BUBBLES

J. D. BUGG AND R. D. ROWE

Department of Mechanical Engineering, The University of Calgary, 2500 University Drive NW, Calgary, Alberta, Canada, T2N 1N4

SUMMARY

A two-dimensional, transient, finite difference technique based on a volume fraction specification of the free surface position and accounting for the effects of surface tension is shown to accurately predict the initial motion of large cylindrical and spherical bubbles. The predictions compare very favourably with the experimental data of Walters and Davidson. The initial acceleration of cylindrical and spherical bubbles is properly predicted as g and $2g$ respectively. The penetration of a tongue of liquid from below is the dominant process by which large deformations from the original shape take place and is well predicted by the model in both cases. For the spherical case the eventual transition into a toroidal bubble is demonstrated and the circulation associated with a rising toroidal bubble as a function of its volume upon release is shown to agree very well with experiments. Iterative linear equation-solving techniques applicable to the special nature of the linear system resulting from such a free surface specification are surveyed and a simple Jacobi iteration based on red–black ordering is found to perform well. The impact of the free surface on the relaxation of the linear system and the convergence criteria is also explored.

KEY WORDS Bubbles Finite difference Initial motion

INTRODUCTION

Like most numerical work requiring 'large' digital computers, the study of bubble dynamics in the numerical laboratory is a relatively recent frontier in fluid dynamics. Earlier efforts to study this important class of free surface flows have been largely confined to experimental and analytical studies. In this paper, interest is focused on the initial motion of cylindrical and spherical bubbles released from rest in quiescent fluids. Furthermore, these bubbles are considered large (>1 cm diameter) and undergo substantial deformations shortly after release. Some experimental data are available against which the model's performance can be evaluated.

The bubble dynamics literature is very extensive because of the importance of bubbles in many chemical and heat transfer processes. However, research has been largely confined to rather small bubbles (<5 mm diameter) where surface tension and viscous effects are very important; for example, Harper[1] provides a comprehensive review of small-bubble behaviour. As the bubble's radius a_0 increases, buoyant forces become more dominant and the hydrostatic pressure gradient becomes important. This paper deals with large air bubbles in water where the Eotvos number $E=100$–1000. Large bubbles are relatively unstable owing to the rapid growth of disturbances on their surfaces. They are of interest in such applications as underwater detonations,[2,3] fluidized beds,[4] nuclear reactor accident analysis[5,6] and the blow-out of undersea oilwells.[7]

In order to place the existing literature and current research in context, consider the three stages of motion of a large cylindrical bubble released from rest in a quiescent liquid. Initially, the bubble

0271–2091/91/110109–21$10.50

Received October 1989

accelerates upwards under the force of buoyancy with little change from its original cylindrical shape. During the second stage it undergoes large deformations until it forms a cylindrical cap (and, perhaps, some small satellite bubbles) which eventually rises at some steady velocity during the final stage. Large spherical bubbles behave similarly but produce a spherical cap and/or a toroidal bubble in the final flow stage. This paper is concerned with the motion of large bubbles during the first and second stages. No attempt is made to model steady cylindrical or spherical cap bubbles.

Experimental literature

The experiments most relevant to this paper are those of Walters and Davidson[8] concerned with cylindrical bubbles and those of Walters and Davidson[9] dealing with spherical bubbles. They provide position and deformation data versus time for the initial stages of motion. As well, they contain photographs of the bubbles well into the large-deformation stage. These works provide the primary source of experimental data against which the model will be compared and as such will be discussed in more detail later.

Davies and Taylor[10] were the first to explain the observed spherical upper surface of spherical cap bubbles as a balance between the dynamics of the flow and gravity which preserves the constant-pressure condition. Experiments with rising spherical cap bubbles led to the relationship $U=\frac{2}{3}\sqrt{(ga)}$ for the terminal velocity of spherical cap bubbles. Studies of the wake structure behind steadily rising cylindrical and spherical cap bubbles have been reported in several papers.[11–14] Bessler and Littman[15] produced cylindrical cap bubbles by the same technique as Walters and Davidson[8] but report no data until the terminal velocity had been reached. However, the steady flow stage focused on in these works is not the main interest, or strength, of the current model.

Several papers dealing with large-bubble dynamics examine the continuous ejection of gas from a submerged orifice. This is a much more complicated problem because it contains a bubble growth process, a departure process and significant bubble-to-bubble interaction. However, since the large-bubble literature is quite limited, the work of Chen and Dhir,[6] Topham[7] and Marble *et al.*[5] should also be mentioned here.

Theoretical literature

The most noteworthy theoretical treatment of the initial motion of large bubbles is the work of Walters and Davidson.[8,9] Their analysis is based on defining the velocity potential for flow around a cylindrical/spherical bubble. This velocity potential is an infinite series, with the first term being the well-known potential for a solid cylinder/sphere in a uniform stream. The remaining terms of the series have time-dependent coefficients. The basis of their methods is to determine these coefficients such that the condition of uniform pressure at the bubble surface is satisfied. They found that the initial acceleration of a cylindrical bubble released from rest is g while for a spherical bubble it is $2g$. Also, a tongue of liquid is found to penetrate the bottom of the bubble. Because of the truncation of the infinite series defining the velocity potential, the analysis is only valid for small deviations from the original shape or until the bubble moves about one bubble radius.

Virtually every other theoretical treatment of large-bubble dynamics is concerned with the terminal velocity or wake structure of cylindrical and spherical cap bubbles. Since these are concerned only with the final, steady stage of motion, individual contributions will not be detailed here. A review of these phenomena has been provided by Wegener and Parlange.[16]

Numerical literature

Numerical investigations of large-bubble movement through liquids are quite recent. Several approachs are apparent in the literature. The first is the vortex-in-cell method. This technique has evolved from the original Lagrangian vortex interaction calculations of Rosenhead[17] to the modern vortex-in-cell technique where the vortex elements are moved by solving the stream function–vorticity equation on an underlying grid. The use of an underlying grid requires only $O(N \ln N)$ operations per time step whereas the original technique of summing over each vortex element requires $O(N^2)$ operations per time step[18] (N being both the number of cells and the number of vortex elements since they are of the same order for simulations with highly distorted surfaces). In bubble calculations the density interface is represented by a series of point vortices whose strength is determined by the vorticity-generating misalignment of the pressure and density gradients. Simulations by Brecht and Ferrante[19] and previously by Meng and Thomson[20] chronicle an impressive range of bubble movement predictions, including important studies of various bubble-to-bubble interactions. However, they consider quite low density ratios (maximum $\rho_1/\rho_2 = 32$) while the current research is concerned with air–water simulations where $\rho_1/\rho_2 \approx 1000$.

Another approach is boundary-fitting finite difference techniques where an orthogonal grid is generated to give a constant co-ordinate value on the bubble surface. This formulation makes the free surface boundary condition relatively simple to apply since co-ordinate lines are perpendicular to the surface and all control volumes are either completely full or completely empty. Ryskin and Leal[21,22] describe such a technique applied to the steady flow around a spherical cap bubble using a stream function–vorticity formulation. They restricted their study to the steady flow stage and therefore did not model the initial stages of motion. The maximum Reynolds number considered was 200.

An alternative approach, used in this paper, makes no attempt to fit the co-ordinate system to the bubble surface but allows the free surface to assume any orientation relative to the co-ordinate lines. This makes the free surface boundary condition more difficult to assign and results in some partially full control volumes. The SOLA-VOF code[23] descended from the MAC[24] (marker-and-cell) technique uses this approach. The advantages are more generality in the free surface configuration and elimination of the curvilinear orthogonal grid as an unknown in the solution. The difficulties arise in convecting the free surface position in a physically realistic manner.

ANALYSIS

The model in this paper uses the SOLA-VOF[23] approach to determine the position of the air-water interface. It is a finite difference technique which advances explicitly in time and uses a pressure correction technique to drive $\nabla \cdot \mathbf{u}$ to zero. All simulations in this paper were done on a uniform grid ($\delta x = \delta y = \text{constant}$).

Full control volumes

The following discretized form of the Navier–Stokes equations is used:

$$u_{ij}^{n+1} = u_{ij}^{n} - \delta t\, C_{x_{ij}}^{n} - \delta t\, V_{x_{ij}}^{n} - \frac{\delta t}{\delta x \rho}\left(P_{i+1,j}^{n+1} - P_{ij}^{n+1}\right), \tag{1}$$

$$v_{ij}^{n+1} = v_{ij}^{n} - \delta t\, C_{y_{ij}}^{n} - \delta t\, V_{y_{ij}}^{n} - \frac{\delta t}{\delta y \rho}\left(P_{i,j+1}^{n+1} - P_{ij}^{n+1}\right). \tag{2}$$

The convective terms have been grouped into C_{ij} and the viscous terms have been grouped into V_{ij}. The viscous terms are always central differenced while the differencing scheme for the convection term is varied between central and upwind differencing depending upon the strength of the convection. This equation set is not closed because continuity has not yet been imposed. This is done by first estimating the velocity field and then correcting it by adjusting the pressure field to satisfy continuity. Details of this process can be found in Reference 25. The result is a linear equation for the pressure correction terms:

$$\Delta P_{ij} - \frac{\Delta P_{i-1,j}}{2[1+(\delta x/dy)^2]} - \frac{\Delta P_{i+1,j}}{2[1+(\delta x/dy)^2]} - \frac{\Delta P_{i,j-1}}{2[1+(\delta y/\delta x)^2]} - \frac{\Delta P_{i,j+1}}{2[1+(\delta y/\delta x)^2]} = -\frac{\rho D_{ij}^g \delta x^2 \delta y^2}{2\delta t(\delta x^2+\delta y^2)}. \tag{3}$$

This equation can be written for each control volume in the solution domain and contains five unknown pressure corrections.

Surface control volumes

The above procedure is valid only for control volumes that are full of liquid. Since this code has the capability of tracking free surfaces, control volumes containing free surfaces must apply the free surface boundary condition in the interior of the solution domain. The free surface boundary condition is

$$\frac{\partial s_{nn}}{\partial \hat{n}} = 0, \tag{4}$$

where $\hat{n}$ is normal to the free surface and s_{nn} is the normal stress in that direction. At the surface this means that

$$P_g + \kappa\sigma = P_s - 2\mu\frac{\partial u_n}{\partial n}, \tag{5}$$

where P_g is the bubble gas pressure, κ is the local surface curvature, σ is the surface tension and P_s is the liquid side pressure. However, since

$$\frac{\kappa\sigma}{\mu(\partial u_n/\partial n)} = O\left(\frac{\sigma}{\mu U}\right) = O\left(\frac{\sigma}{\mu\sqrt{(ga_0)}}\right) = O(100), \tag{6}$$

the viscous term can be neglected, giving

$$P_s = P_g + \kappa\sigma. \tag{7}$$

The goal is to set the surface cell pressure such that it will result in a surface pressure of P_s when linearly interpolated to the neighbouring full cell (see Figure 1). We want

$$P_{ij}^{n+1} = \eta_{ij} P_s + (1-\eta_{ij}) P_{pq}^{n+1}. \tag{8}$$

However, the linear system is in ΔP, so to express (8) in a form consistent with full cells, it is written as

$$\Delta P_{ij} + (\eta_{ij}-1)\Delta P_{pq} = \eta_{ij} P_s + (1-\eta_{ij}) P_{pq}^n - P_{ij}^n. \tag{9}$$

The solution of (3) and (9) is the largest task facing the model. Several techniques have been pursued in the light of the special problems imposed by the free surface. The first influence of equation (9) is that it renders the coefficient matrix asymmetric. This increases the storage requirements greatly and rules out solvers which rely on symmetric coefficient matrices. The

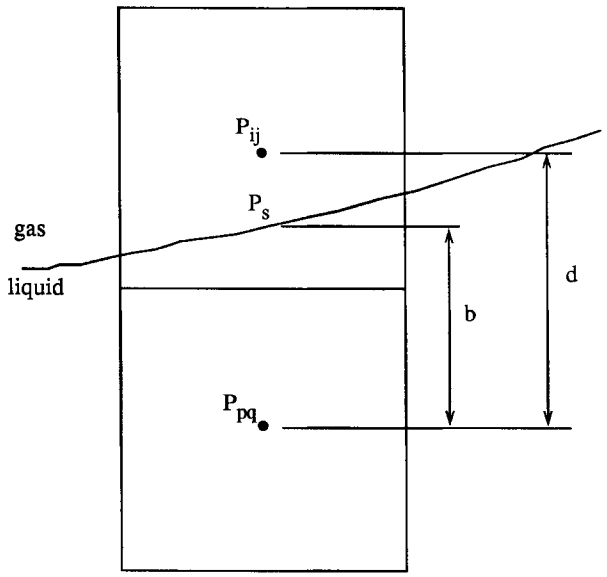

Figure 1. Surface pressure interpolation technique ($\eta_{ij}=d/b$)

second and most serious consequence of (9) is that it introduces severe numerical instabilities when η_{ij} is greater than two by violating diagonal dominance. A full discussion of the solution techniques implemented in the light of these problems is provided below.

Convecting the free surface

The free surface position is defined in terms of a volume fraction F, which is unity in full control volumes, zero in empty control volumes and takes intermediate values in surface control volumes. The process of updating F at the end of each time step convects the free surface and is governed by

$$\frac{\partial F}{\partial t}+u\frac{\partial F}{\partial x}+v\frac{\partial F}{\partial y}=0. \tag{10}$$

Numerical interpretation of this equation must ensure that the interface remains sharply defined and therefore a special donor–acceptor method is used. A good discussion of this technique can be found in Reference 26.

Stability considerations

The linear interpolation which specifies the free surface boundary condition can lead to a numerical instability when iteratively solving the linear equation set. If η_{ij} is greater than two, diagonal dominance will be lost, causing the iterative scheme to diverge. In this work a relaxation factor of $\omega_{pq}=0{\cdot}9/(\eta_{ij}-1)$ is applied to all cells where $\eta_{ij}>2$. Note that since it is the ΔP_{pq} coefficient and not the ΔP_{ij} coefficient that creates the instability, the relaxation is applied in cell pq. All other cells are not relaxed in this solution.

Ordering schemes

A large portion of the computational effort is the solution of equations (3) and (9) for the pressure correction ΔP. Equation (3) has five non-zero members in each row of the coefficient matrix. The structure of the coefficient matrix is dependent on the ordering scheme.[27] Figure 2 shows a very small grid ($nx=7$, $ny=6$) with the control volumes numbered according to three different ordering schemes. By using ordering schemes to change the structure of the coefficient matrix, more efficient iterative techniques may be implemented.

Natural ordering. First consider natural ordering. Since the differencing molecule yields only five unknowns per equation and the order of the set is typically 10^4, the coefficient matrix is obviously very sparse. For an $nx \times ny$ grid, all elements a_{ij} are zero except when $j=i$, $j=i-1$, $j=i+1$, $j=i-nx$ and $j=i+nx$. Therefore **A** has a pentadiagonal structure with a half-bandwidth of nx.

$$\mathbf{A}\Delta\mathbf{P}=\mathbf{b}. \tag{11}$$

Because equation (3) is normalized, the diagonal members of **A** are all unity.

Red–black point ordering. When the coefficient matrix is constructed using red–black point ordering, it may be partitioned as

$$\begin{bmatrix} \mathbf{I} & \mathbf{G}_b \\ \mathbf{G}_r & \mathbf{I} \end{bmatrix} \begin{bmatrix} \Delta\mathbf{P}_r \\ \Delta\mathbf{P}_b \end{bmatrix} = \begin{bmatrix} \mathbf{b}_r \\ \mathbf{b}_b \end{bmatrix}. \tag{12}$$

The submatrices on the diagonal are identity matrices and $\mathbf{G}_b$ and $\mathbf{G}_r$ each have four non-zero members per row. Because of this partitioning, the solution vector $\Delta\mathbf{P}$ is also partitioned into $\Delta\mathbf{P}_r$ and $\Delta\mathbf{P}_b$, the red and black solutions. This ordering scheme derives its name from the checkerboard-like pattern that the two solutions create. The structure of the partitioned coefficient matrix arises from the fact that no red control volume has another red control volume as its neighbour. Therefore each half of the solution is explicit and they are linked through $\mathbf{G}_r$ and $\mathbf{G}_b$.

Red–black line ordering. Red–black line ordering allows a similar partitioning (equation (13)), but $\mathbf{H}_r$ and $\mathbf{H}_b$ are tridiagonal matrices and $\mathbf{G}_r$ and $\mathbf{G}_b$ each have only two members per row.

$$\begin{bmatrix} \mathbf{H}_r & \mathbf{G}_b \\ \mathbf{G}_r & \mathbf{H}_b \end{bmatrix} \begin{bmatrix} \Delta\mathbf{P}_r \\ \Delta\mathbf{P}_b \end{bmatrix} = \begin{bmatrix} \mathbf{b}_r \\ \mathbf{b}_b \end{bmatrix}. \tag{13}$$

36	37	38	39	40	41	42
29	30	31	32	33	34	35
22	23	24	25	26	27	28
15	16	17	18	19	20	21
8	9	10	11	12	13	14
1	2	3	4	5	6	7

(a)

39	19	40	20	41	21	42
15	36	16	37	17	38	18
32	12	33	13	34	14	35
8	29	9	30	10	31	11
25	5	26	6	27	7	28
1	22	2	23	3	24	4

(b)

36	37	38	39	40	41	42
15	16	17	18	19	20	21
29	30	31	32	33	34	35
8	9	10	11	12	13	14
22	23	24	25	26	27	28
1	2	3	4	5	6	7

(c)

Figure 2. Ordering scheme: (a) natural; (b) red–black point; (c) red–black line

Each half of the solution can be solved by a fast direct method (tridiagonal matrix algorithm) and it is linked more weakly with the other half of the solution since $\mathbf{G}_r$ and $\mathbf{G}_b$ each have only two members per row.

Basic iterative methods

Now that the ordering schemes have been discussed, some basic iterative methods can be introduced. Not all of these basic iterative methods are used with all possible ordering schemes, but several combinations are discussed and compared in this paper.

Jacobi iterative scheme. The simplest of all iterative schemes is the Jacobi iterative technique shown in equation (14). Every member of the solution is updated based entirely on the solution at the previous iteration. The disadvantage of this technique is that its explicit nature leads to rather slow convergence. However, in terms of vectorization it is very attractive since it is directly vectorizable. The trade-off between poor convergence properties and amiability to vector hardware will determine this method's utility.

$$\Delta \mathbf{P}^{m+1} = \mathbf{b} - (\mathbf{A} - \mathbf{I})\Delta \mathbf{P}^m. \tag{14}$$

Gauss–Seidel iterative scheme. The next technique is the Gauss–Seidel iterative scheme. In this scheme, two of the four neighbour terms in each equation are evaluated at the current iteration. This makes it converge much more quickly than the Jacobi technique since it is more implicit. However, it is much less suitable for vectorization because of its recursive nature. It is a very attractive method on scalar hardware using the natural ordering scheme, since it merely involves stepping through the grid and updating the solution based on the current state of the solution vector.

$$\Delta \mathbf{P}^{m+1} = (\mathbf{I} + \mathbf{C}_L)^{-1}(\mathbf{b} - \mathbf{C}_U \Delta \mathbf{P}^m), \tag{15}$$

where $\mathbf{C}_L$ is the lower triangular portion of $\mathbf{A}$ and $\mathbf{C}_U$ is the upper triangular portion of $\mathbf{A}$.

Tridiagonal matrix algorithm. The tridiagonal matrix algorithm (TDMA) is not in itself an iterative technique. It is a direct solver of a special class of linear systems having tridiagonal coefficient matrices. However, if we make each iteration a tridiagonal problem by moving the contribution of two neighbours into the constant vector, an iterative technique can be developed that has good convergence properties for many problems. Equation (16) describes this method.

$$\Delta \mathbf{P}^{m+1} = \mathbf{K}^{-1}(\mathbf{b} - \mathbf{C}_B \Delta \mathbf{P}^m), \tag{16}$$

where $\mathbf{A} = \mathbf{K} + \mathbf{C}_B$ and $\mathbf{K}$ is the tridiagonal portion of $\mathbf{A}$. Information is transmitted along the lines that define the TDMA in one iteration whereas information is transmitted across the TDMA lines at a rate of one grid cell per iteration. Therefore alternating the sweeping direction usually speeds up the solution substantially.[28]

Speed comparison

To compare the speed of the five solvers, the case of a cylindrical bubble released from rest is used. A complete description of these simulations is presented in the next section. The solution domain is 61×160 control volumes, resulting in a matrix of order 9760, and the first 25 time steps are benchmarked to produce Table I. The convergence criterion ε for these runs is 10^{-6} and the time step is 0·0002 s. Quantities in square brackets are relative to the Jacobi scheme with red–black ordering (method IV in Table I).

Table I. Speed comparison of five linear equation solvers

Method	Ordering	Basic iterative technique	Set-up time (ms)	Time per iteration (ms)	Floating point operation per iteration	Rate (Mflops)	Total iterations	Total time (s)
I	Natural	Jacobi	1·69 [0.31]	2·04 [1·33]	165920 (17N)	79·0	75121 [17·1]	152·9 [22·2]
II	Natural	Gauss–Seidel	2·94 [0·55]	10·93 [7·14]	224480 (23N)	20·5	2488 [0·56]	27·26 [3·96]
III	Natural	TDMA	8·16 [1·52]	3·84 [2·51]	283040 (—)	73·7	2777 [0·63]	10·87 [1·58]
IV	RB Point	Jacobi	5·38 [1·00]	1·53 [1·00]	131760 (13·5N)	86·7	4404 [1·00]	6·883 [1·00]
V	RB Line	TDMA	8·89 [1·65]	3·41 [2·23]	200080 (—)	58·7	2262 [0·51]	7·946 [1·15]

The set-up time in Table I includes such things as zeroing the solution vector(s), initializing the bit mask vectors for full cells and red–black cells if applicable, loading the relaxation vectors, pre-relaxing the coefficient matrix and constant vector and loading the vectors required for the convergence check. For those techniques which use the tridiagonal matrix algorithm, the set-up time includes the coefficient matrix decomposition stage, which explains the large set-up times for methods III and V.

The time per iteration includes both the solution and convergence check stages. Methods using the easily vectorizable Jacobi iterative technique (I and IV) are the fastest running. Two factors give rise to the differences between methods I and IV. Method IV is made slightly slower by the fact that the vector length is half that of method I. However, this is more than offset by the fact that the convergence check is usually half as large for method IV. The large time for method II results from the solution stage being only 50% vectorized (the convergence check is 100% vectorized).

The floating point operations per iteration are obtained by counting the operations in the iteration loop of the solver. The actual tridiagonal matrix solver in methods III and V is from the MAGEV[29] library of subroutines and the number of floating point operations does not vary linearly with N as for the other methods. The rate in Mflops is simply calculated from the time per iteration and the number of operations. A two-pipe Cyber 205 was used for this study, and with no linked triads, the maximum speed realizable using single precision is 100 Mflops. Degradation of this rate is due to vectorizability of different methods, vector set-up time and scalar overhead such as incrementing the iteration counter and deciding whether to iterate again.

A favourable method must not only be able to complete an iteration quickly but must also be able to obtain a converged solution in a competitive number of iterations. These two factors combine to yield the total time for this particular benchmark solution. Whereas the running speed of each method is basically independent of the case being run, the number of iterations required may depend heavily on the details of the problem being solved. The code is structured so that the assembly of the coefficient matrix and constant vector is independent of the solution method selected. This makes it very easy to change solution methods. This capability is strongly recommended, since different solvers may perform better in different cases. On the basis of this study, the favoured method for this application is the Jacobi iterative technique based on the red–black point-ordering scheme.

Relaxation technique

Methods I, II and IV use pre-relaxation to slightly reduce the number of floating point operations inside the iteration loop. Pre-relaxation is the practice of performing a portion of the relaxation procedure before the solution by relaxing the coefficient matrix and constant vectors. Illustrating this with method I:

post-relaxation

$$\Delta\mathbf{P}^{m+(1/2)} = \mathbf{b} - [(\mathbf{A} - \mathbf{I})]\Delta\mathbf{P}^{m}, \tag{17}$$

$$\Delta\mathbf{P}^{m+1} = \omega\Delta\mathbf{P}^{m+(1/2)} + (1-\omega)\Delta\mathbf{P}^{m}; \tag{18}$$

pre-relaxation

$$\Delta\mathbf{P}^{m+(1/2)} = [\omega\mathbf{b}] - [\omega(\mathbf{A} - \mathbf{I})]\Delta\mathbf{P}^{m}, \tag{19}$$

$$\Delta\mathbf{P}^{m+1} = \Delta\mathbf{P}^{m+(1/2)} + (1-\omega)\Delta\mathbf{P}^{m}. \tag{20}$$

The quantities in square brackets can be calculated before iteration begins. Therefore inside the iteration loop this technique saves one floating point operation per control volume, namely the $\omega\Delta\mathbf{P}^{m+(1/2)}$ product in equation (18).

Convergence criteria

A problem with iterative linear equation solvers is deciding when to stop the iteration procedure and accept the current solution. This decision demands a large part of the total time of many iterative techniques. Also, the presence of relaxation factors in the solution must be accounted for by the convergence criteria. To illustrate the formulation of the convergence criteria, consider the Jacobi technique based on red–black point ordering and using the pre-relaxation technique.

$$\Delta\mathbf{P}_r^{m+(1/2)}=\omega_r\mathbf{b}_r-\omega_r\mathbf{G}_b\Delta\mathbf{P}_b^m, \tag{21}$$

$$\Delta\mathbf{P}_r^{m+1}=\Delta\mathbf{P}_r^{m+(1/2)}+(1-\omega_r)\Delta\mathbf{P}_r^m, \tag{22}$$

$$\Delta\mathbf{P}_b^{m+(1/2)}=\omega_b\mathbf{b}_b-\omega_b\mathbf{G}_r\Delta\mathbf{P}_r^{m+1}, \tag{23}$$

$$\Delta\mathbf{P}_b^{m+1}=\Delta\mathbf{P}_b^{m+(1/2)}+(1-\omega_b)\Delta\mathbf{P}_b^m. \tag{24}$$

Assume that $\Delta\mathbf{P}=[\Delta\mathbf{P}_r^{m+1},\Delta\mathbf{P}_b^m]^T$ represents a converged solution. Then the residuals can be calculated from

$$\Delta\mathbf{P}_r^{m+1}=\mathbf{b}_r^{m+1}-\mathbf{G}_b\Delta\mathbf{P}_b^m, \tag{25}$$

$$\Delta\mathbf{P}_b^m=\mathbf{b}_b^{m+1}-\mathbf{G}_r\Delta\mathbf{P}_r^{m+1}, \tag{26}$$

where $\mathbf{b}_r^{m+1}$ and $\mathbf{b}_b^{m+1}$ should ideally equal $\mathbf{b}_r$ and $\mathbf{b}_b$. Multiplying (25) and (26) by ω_r and ω_b respectively, subtracting from (21) and (22) and recalling the definition of $\mathbf{b}_r$ and $\mathbf{b}_b$ gives

$$\Delta\mathbf{P}_r^m-\Delta\mathbf{P}_r^{m+1}=\frac{\omega_r}{(1-\omega_r)}\frac{\rho\delta x^2\delta y^2}{2\delta t(\delta x^2+\delta y^2)}(\mathbf{D}_r^g-\mathbf{D}_r^{m+1}), \tag{27}$$

$$\Delta\mathbf{P}_b^m-\Delta\mathbf{P}_b^{m+1}=\frac{\omega_b\rho\delta x^2\delta y^2}{2\delta t(\delta x^2+\delta y^2)}(\mathbf{D}_b^g-\mathbf{D}_b^{m+1}). \tag{28}$$

The difference on the right-hand side of this expression is the error in divergence at the $(m+1)$th iteration. This can now be compared with the allowable relative volume flow imbalance ε to give the convergence criteria

$$|\Delta\mathbf{P}_r^{m+1}-\Delta\mathbf{P}_r^m|<\frac{\varepsilon\rho\delta x^2\delta y^2\omega_r}{2\delta t^2(1-\omega_r)(\delta x^2+\delta y^2)}, \tag{29}$$

$$|\Delta\mathbf{P}_b^{m+1}-\Delta\mathbf{P}_b^m|<\frac{\varepsilon\rho\delta x^2\delta y^2\omega_b}{2\delta t^2(\delta x^2+\delta y^2)}. \tag{30}$$

The red–black ordering scheme makes it possible to save computation time during the convergence check. Note that (29) is certain to be satisfied in any control volume where $\omega=1$. Therefore criterion (30) is checked first, and only if it is satisfied is there any need to check (29). This means that until very close to convergence only half of the solution needs to be checked for convergence.

Note that the convergence check described above is fully vectorizable. However, since only one control volume need violate the convergence criteria in order to demand another iteration, it may seem more efficient to do a fully scalar convergence check and proceed to the next iteration upon the first violation. Near the beginning of the iterative process, where many control volumes violate

the criteria, this would undoubtedly be faster. However, near convergence, when only a few stubborn residuals remain, it depends on where they are positioned in the solution vector as to which method would be fastest. This is impossible to predict *a priori* in any general way, so the fully vectorized convergence check is retained.

The fact that this code must evaluate the void fraction in each control volume in order to track the movement of the free surface places extra importance on knowing the error in the solution. The routine which updates the void fraction in each control volume at the end of each time step does so by calculating the imbalance of mass flux across the control volume faces. The convergence criteria allow a small imbalance in mass flow to occur. This allowable divergence must be considered in updating the void fraction or new, fictitious void regions may appear merely by virtue of non-zero divergence. Therefore the minimum void fraction $\alpha_{\min}$, which is allowed to appear in a previously full cell is ε.

RESULTS AND DISCUSSIONS

Cylindrical bubbles

The experiments performed by Walters and Davidson[8] provide a good test of the model's capabilities. The initial conditions are achieved by suddenly withdrawing a 50·8 mm diameter sleeve from between two vertical Perspex plates 9·5 mm apart, 254 mm wide and 1·2 m high. The computational domain covers the entire width of the tank but is restricted in height to 0·3387 m, resulting in a 61×160 grid having $\delta x = \delta y = 2{\cdot}11\bar{6}$ mm. The rather narrow width of the column in these experiments is far from the assumption of an infinite expanse of fluid. Studies show that the terminal velocity is reduced by decreasing the channel width,[14] but no work is available on its influence during the initial stages of motion. Walters and Davidson[8] state that the initial bubble pressure is set so that there is 'minimal tendency for a volume change to occur on release'. This is achieved in the model by initializing the bubble pressure to be equal to the hydrostatic pressure at the bubble centroid at $t=0$. Thereafter the bubble pressure is recalculated at each time step according to the isentropic expansion/compression of air in response to changes in bubble volume resulting from updating the surface position. The present work is only intended to model the first two stages of bubble motion since the experimental data[8] are restricted to these stages.

Initial stage. During the initial non-deforming motion the most important quantity to verify is the bubble's acceleration. This can be shown theoretically and has been confirmed experimentally[8] to be equal to the gravitational acceleration g. Figure 3, which shows the bubble position versus time obtained from Walters and Davidson,[8] confirms that the model properly predicts this initial acceleration. Note that for $T = t\sqrt{(g/a_0)} > 1$ the upward motion begins to deviate from constant acceleration as the second phase of motion is approached.

Deformation stage. The second phase of motion, transition to a cylindrical cap, begins with the penetration of a tongue of liquid into the bottom surface of the bubble. This is well predicted by the model and begins at $T \approx 0{\cdot}6$. The predicted streamlines for both a stationary and moving observer are shown at four times during the transition phase in Figure 4. Figure 5 shows the penetration quantitatively by plotting the vertical diameter of the bubble versus time for the period over which experimental data were reported. Also shown in this figure is a curve determined from the potential flow model of Walters and Davidson.[8] The data in Figures 3 and 5 only represent the initial stages of large deformation. Beyond $T = 1{\cdot}4$ the photographic data reported by the experimenters must be used. Figure 6 shows a comparison of the photographs with the model predictions. The photographs clearly show that in the later stages of transition to a

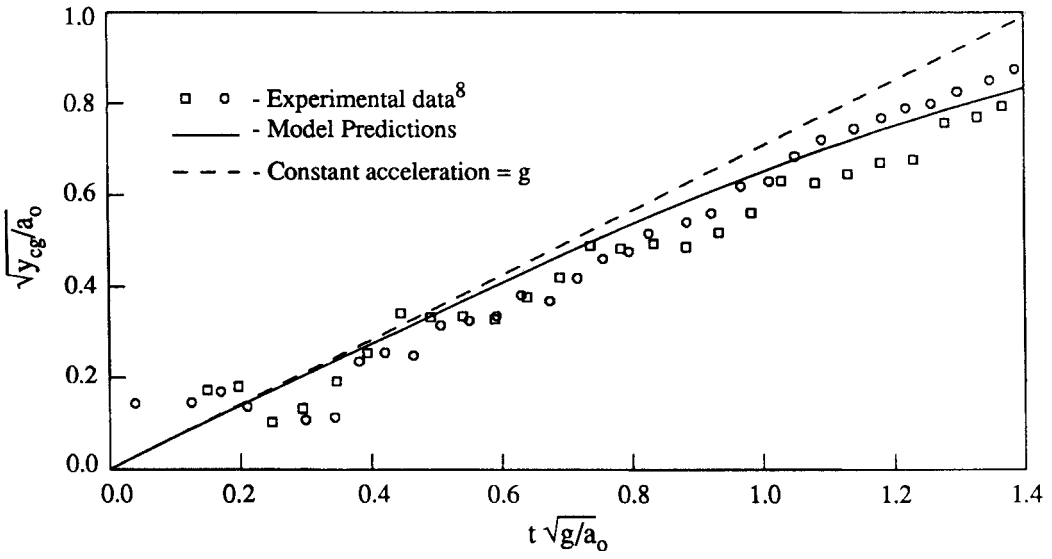

Figure 3. Position versus time for a cylindrical bubble released from rest into a quiescent liquid. Experimental data of Walters and Davidson[8]

steady flow the penetration of liquid from below forms a trailing skirt. In frames 6 and 7 the experimental data show some necking of this trailing skirt. This necking is quite important because it eventually becomes complete and results in a cylindrical cap with two small bubbles in its wake. This shedding is the mechanism by which vorticity is generated in the flow as it transforms from potential flow around a cylinder to fully separated flow behind a cylindrical cap.

The model results do not show such distinct shedding. Very small bubbles are shed from the trailing edge of the skirt but not from a clear necking process. However, the formation of a cylindrical cap with several small bubbles in the wake is very clear in frame 8. Other experiments using the same bubble injection technique[15] reported no trailing bubbles in the wake. However, they only reported data after the cylindrical caps had reached terminal velocity. Since the wake is quite turbulent for an air–water bubble of this size ($Re \approx 26\,700$), the shed bubbles likely recirculate until they coalesce with the cap through its wavy floor and therefore do not consistently appear in the fully developed wake. Model development has not been pursued to the point where it is reasonable to expect turbulent flow in the wake to be accurately predicted since the model has no capacity to model turbulence at this time.

Cylindrical approximation. Recall that the 'cylindrical' bubbles in the experiments were contained between two plates 9·5 mm apart whereas the model is truly two-dimensional. A discussion of wall effects is given in Reference 30 but only as they pertain to the terminal velocity. It was concluded that two-dimensional models underpredict the rise velocity of cylindrical bubbles created between parallel plates. Instability makes it impossible to create truly cylindrical bubbles in the laboratory. It is likely that the 'laboratory' cylindrical bubble has a more stable skirt than the truly two-dimensional bubble owing to the extra curvature present in the third dimension. It is not clear whether the differences in the shedding process are a result of deficiencies in the model or wall effects in the experiments.

Surface tension. The specification of surface tension in the surface boundary condition is very important to the success of this model. The effects of attempting a prediction without the surface

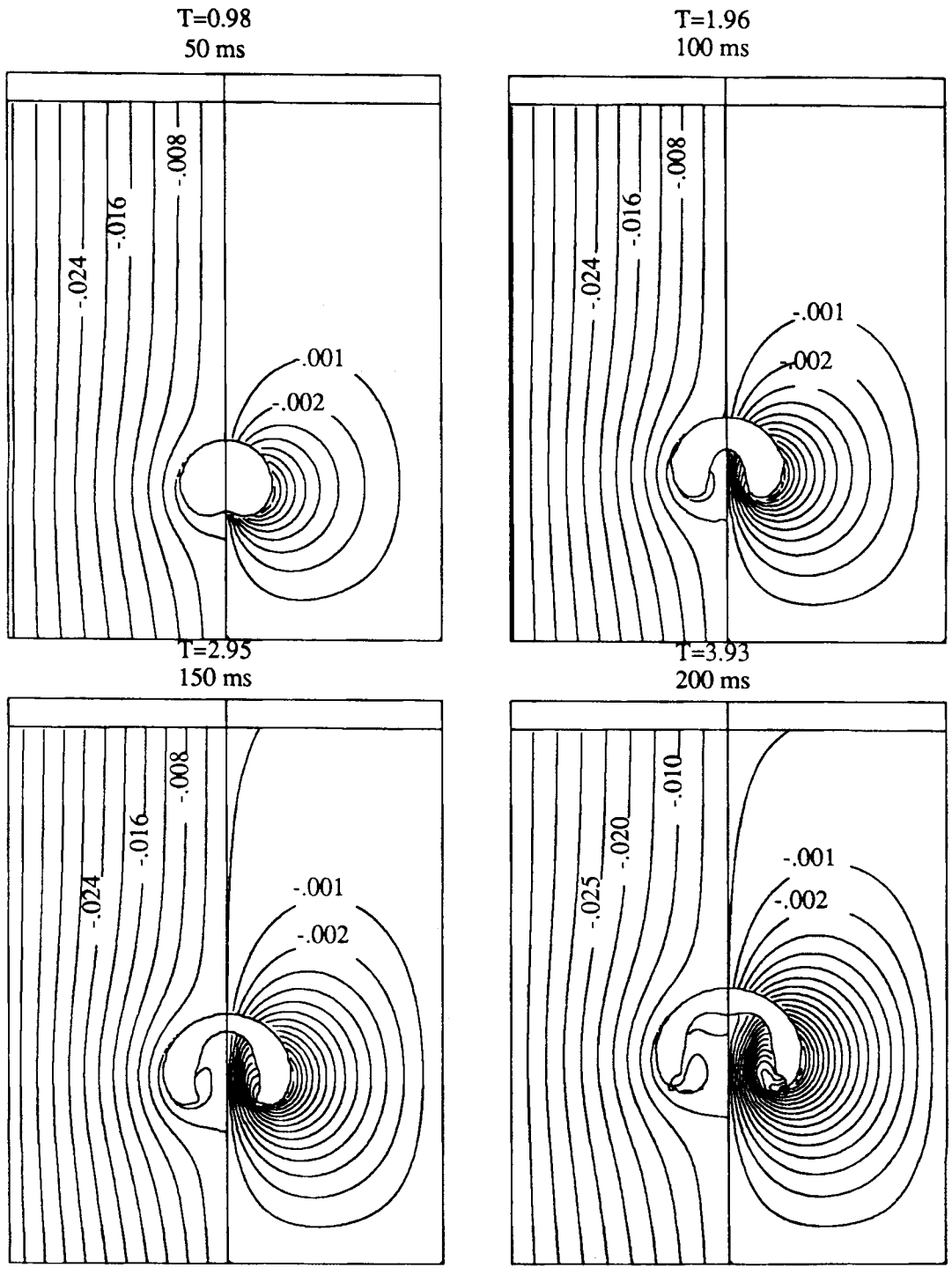

Figure 4. Streamfunction contours for the initial motion of a cylindrical bubble released from rest in a quiescent liquid (uniform contour intervals): right side, stationary observer, left side, observer on bubble

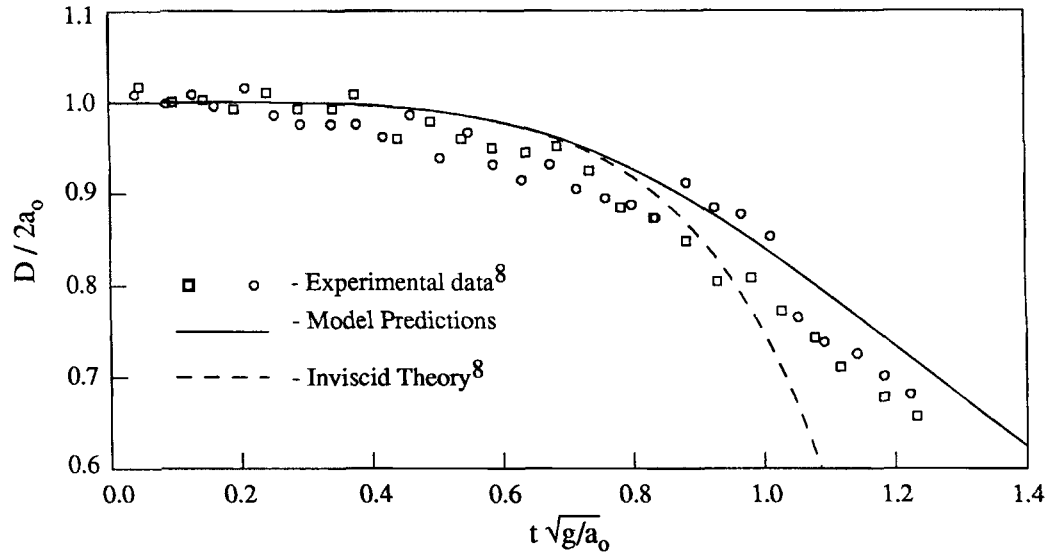

Figure 5. Vertical diameter versus time for a cylindrical bubble released from rest into a quiescent liquid. Experimental data of Walters and Davidson[8]

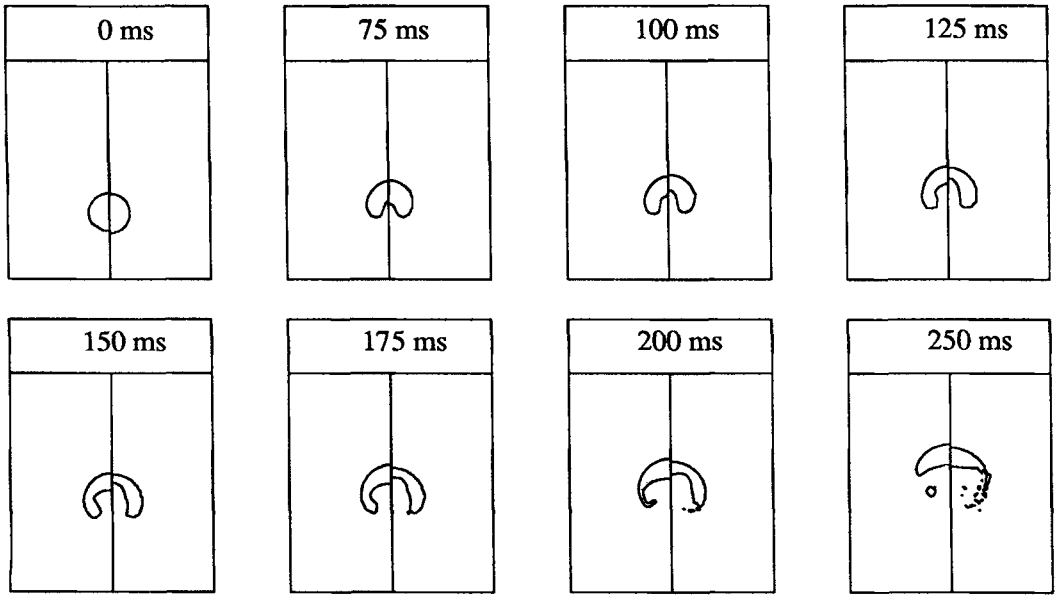

Figure 6. Cylindrical bubble predictions compared to photographs of Walters and Davidson[8]

tension model can be seen in Figure 7. The first difference was observed at the 75 ms point where a small bump began to grow on the top surface of the bubble. This bump continues to grow in the form of a disturbance propagating down the sides of the bubble. This behaviour is very different from the experimental results where the upper surface remains cylindrical. Implementing the

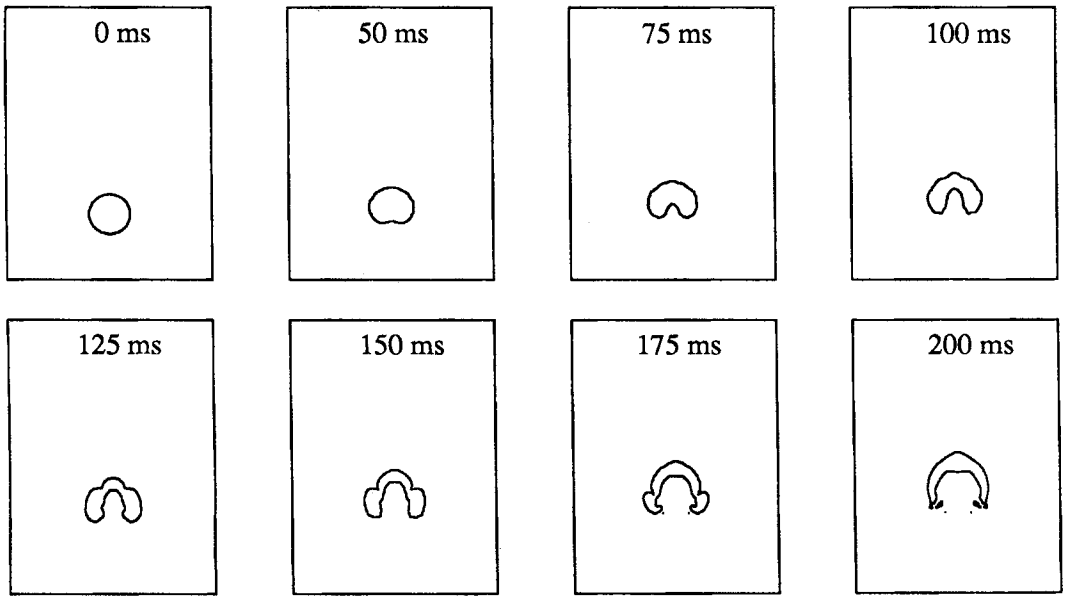

Figure 7. Effect of neglecting surface tension on cylindrical bubble predictions

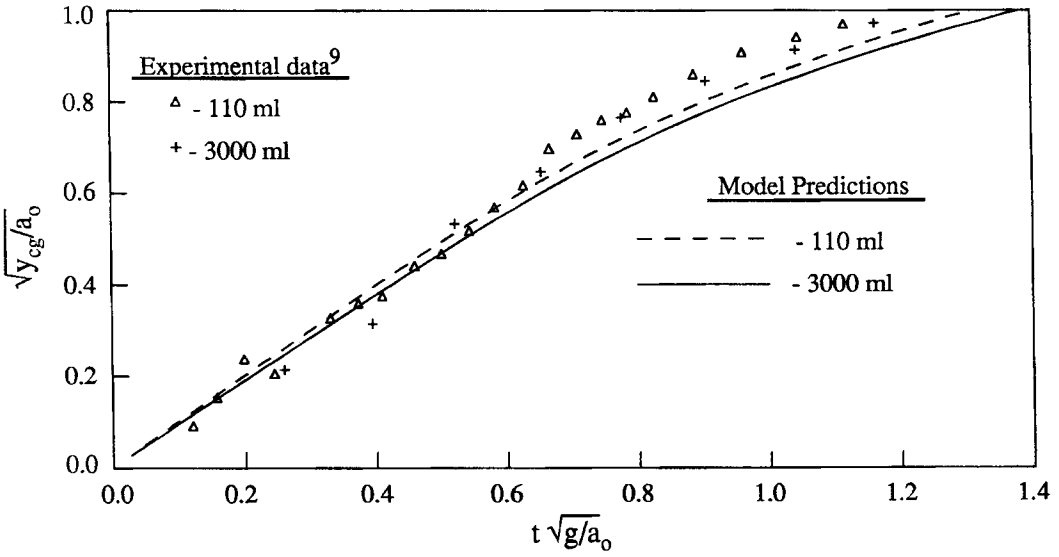

Figure 8. Position versus time for a spherical bubble released from rest into a quiescent fluid. Experimental data of Walters and Davidson[9]

surface tension model eliminated the initial formation of this disturbance, allowing the upper surface to remain cylindrical. Even though surface tension is a relatively small force when the bubble size is large, it is vital to successful solutions, since very small disturbances can otherwise grow unchecked and dominate the features of the bubble.

Grid independence. To investigate the grid independence of the current solution, a much finer grid was developed for the case of the rising cylindrical bubble. A 153 × 408 uniform grid yielding a grid resolution of $\delta x = \delta y = 0{\cdot}836$ mm and an equation set of order 62 424 was run for the first 40 ms ($T = 0{\cdot}79$) of the simulation and showed no appreciable difference in the results up to that point.

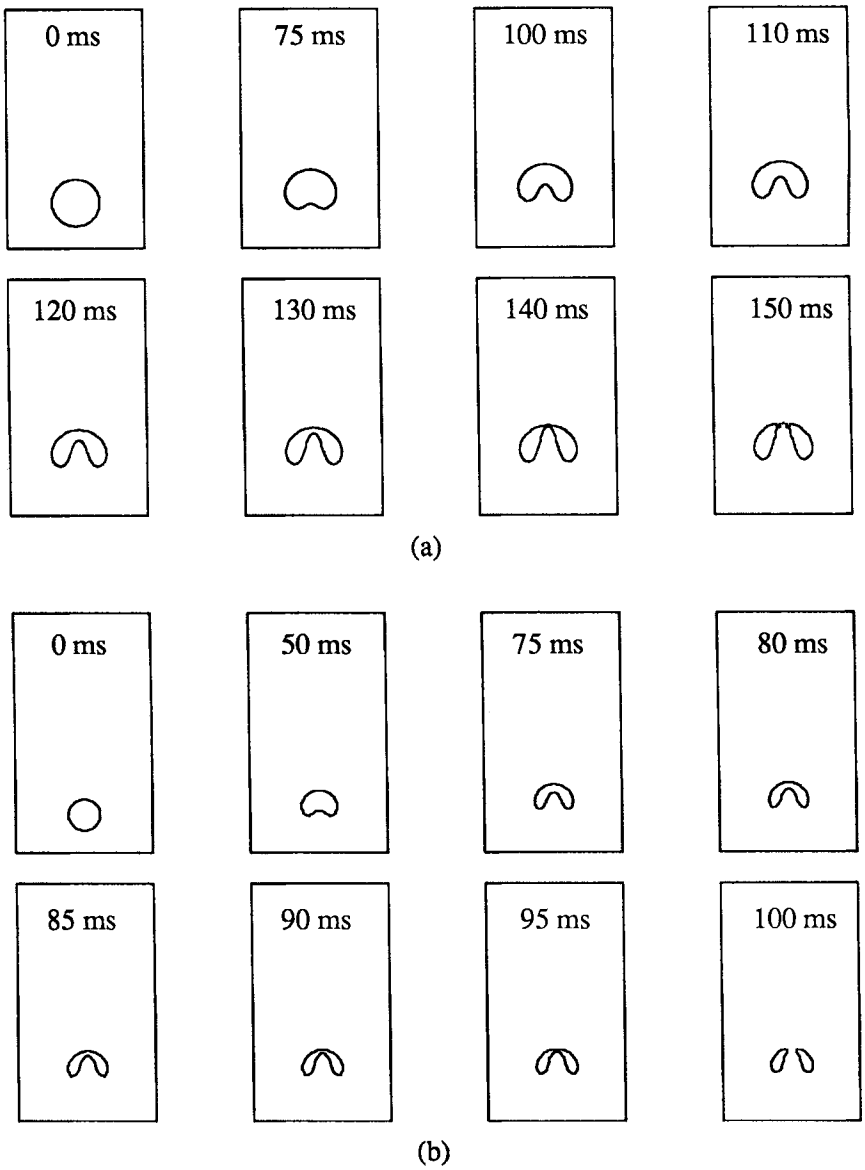

Figure 9. Prediction of initial motion of spherical bubbles released from rest into a quiescent liquid: (a) 3000 ml bubble; (b) 110 ml bubble (shown double size)

Spherical bubbles

Walters and Davidson[9] describe a similar study of initially spherical bubbles. Spherical bubbles ranging in volume from 110 to 3000 ml were released into a 45·7 cm square by 0·91 m high tank. The desired initial condition of a spherical bubble released from rest into a quiescent fluid was attained by bursting inflated balloons of various volumes with a remotely actuated needle while they were submerged in an otherwise liquid-filled container. Upon bursting, the rigidity of the container maintained the constant volume of the bubble.

Initial stage. As with the two-dimensional work, the experimenters reported vertical displacement of the bubble versus time (see Figure 8). Again the model results match the experimental data very well. Note that the initial acceleration of a spherical bubble released from rest is $2g$.

Deformation stage. The penetrating liquid tongue is much harder to see in the photographs[9] because it is obscured by the resulting skirt. This made a direct comparison of the bubble silhouettes difficult in this case, so the model results alone are presented in Figure 9 for initial bubble volumes of 110 and 3000 ml. The beginning of the large-deformation stage is again best characterized by plotting the vertical diameter versus time as in Figure 10. The break-up resulting from penetration was into a very small spherical cap (often zero volume) and a rather large toroidal bubble.[9] This contrasts with the cylindrical case where the cap inherited the bulk of the initial volume. Because of this, no modelling of spherical cap bubbles was done. This would require a different set of initial conditions. Experimental studies of spherical caps usually use a dump cup mechanism.[10]

Toroidal bubble formation

The second part of Reference 9 is concerned with the formation of a toroidal bubble. Air was injected into a tank to form toroidal bubbles of various volumes. After the bubble formed, by penetration of a tongue of liquid from below, Walters and Davidson measured the circulation

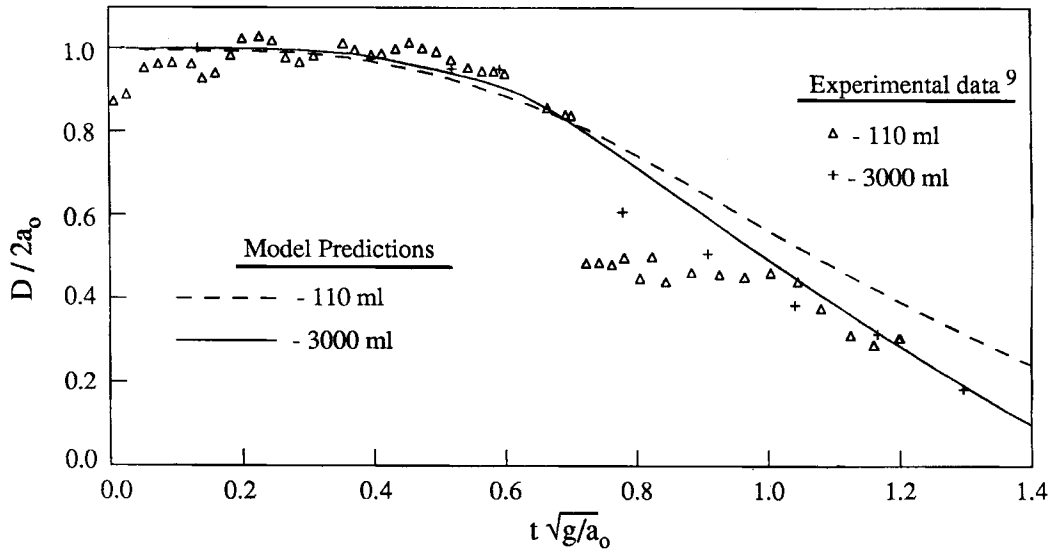

Figure 10. Vertical diameter versus time for a spherical bubble released from rest into a quiescent liquid. Experimental data of Walters and Davidson[9]

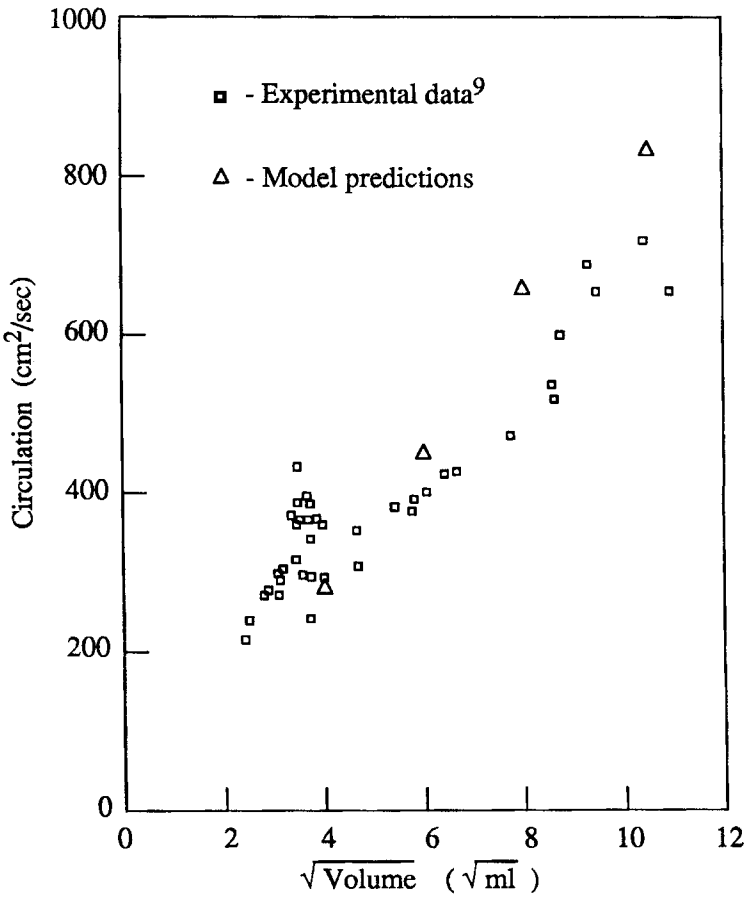

Figure 11. Circulation associated with toroidal bubble versus bubble volume. Experimental data of Walters and Davidson[9]

associated with the bubble by assuming it to be the core of a ring vortex. They found this circulation to be essentially constant as the bubble rose, with its ring diameter increasing and toroid diameter decreasing. Using the numerical technique described in this paper, spherical bubbles of various volumes (comparable to those in the experiments) were released and allowed to form into toroids. The circulation around these bubbles is easily computed from the velocity field and was found to be essentially constant after the toroid was formed. The Walters and Davidson[9] data for circulation versus the square root of the bubble volume are shown in Figure 11 along with the model results.

CONCLUSIONS

The present finite difference model has been shown to effectively predict the initial motion of large gas bubbles released from rest in quiescent fluids. The impact of having a free surface in the interior of the solution domain has been considered in formulating the convergence criteria and selecting iterative equation solvers. Further work is required to model the turbulent wake behind rising gas

bubbles, which occurs later in their existence, and allow physically realistic break-up and coalescence to occur.

ACKNOWLEDGEMENTS

This project has been supported by a contract from the Environmental Emergencies Technology Division of Environment Canada and an operating grant from the Canadian Natural Sciences and Engineering Research Council. J.D.B. is grateful for the award of a Killam Memorial Scholarship.

APPENDIX: NOMENCLATURE

$\mathbf{A}$	coefficient matrix
a	radius of curvature of bubble's leading edge
$\mathbf{b}$	constant vector
$\mathbf{C}$	portion of $\mathbf{A}$
D	divergence in control volume
E	Eotvos number, $4ga_0^2\rho/\sigma$
F	volume fraction of fluid
g	acceleration due to gravity
$\mathbf{G}$	submatrix of $\mathbf{A}$
$\mathbf{H}$	submatrix of $\mathbf{A}$
$\mathbf{I}$	identity matrix
$\mathbf{K}$	tridiagonal portion of $\mathbf{A}$
nx	number of control volumes in x-direction
ny	number of control volumes in y-direction
N	order of linear equation set
P	pressure
Re	Reynolds number
s	stress
t	time
T	dimensionless time $t\sqrt{(g/a_0)}$
u	velocity in x-direction
U	dimensionless velocity
v	velocity in y-direction

Greek symbols

α	void fraction
ΔP	pressure correction
δx	grid spacing in x-direction
δy	grid spacing in y-direction
ε	convergence criterion
Γ	circulation
κ	curvature
μ	dynamic viscosity
η	interpolation factor
ρ	liquid density

σ	surface tension
ω	relaxation factor

Subscripts

b	black
0	time zero
ij	control volume index
L	lower
pq	control volume index
r	red
s	at surface
U	upper

Superscripts

g	guess
m	iteration number
$m+(1/2)$	unrelaxed
n	time step number

REFERENCES

1. J. F. Harper, 'The motion of bubbles and drops through liquids', *Adv. Appl. Mech.*, **12**, 59–129 (1972).
2. Lord Rayleigh, 'On the pressure developed in a liquid during the collapse of a spherical cavity', *Phil. Mag., Ser. 6*, **34**, 200 (1917).
3. S. A. Wilkerson, 'Boundary integral techniques for explosion bubble collapse', *Energy Sources Technology Conf. and Exhibition*, Houston, ASME Paper No. 89-OCN-2, 22–25 January 1989.
4. R. Cliff, J. R. Grace and M. E. Weber, 'Stability of bubbles in fluidized beds', *Ind. Chem. Eng. Fund.*, **13**, 45–51 (1974).
5. W. J. Marble, T. L. Wong, F. J. Moody and D. A. Hankins, 'Retention of fission products by BWR suppression pools during severe reactor accidents', *Int. Thermal Nuclear Reactor Safety Conf.*, Chicago, 1982.
6. C. L. Chen and V. K. Dhir, 'Hydrodynamics of a bubble formed at vent pipe exit', *Int. J. Multiphase Flow*, **8**, 147–163 (1982).
7. D. R. Topham, 'Hydrodynamics of an oilwell blowout', *Beaufort Sea Technical Report 33*, 1975.
8. J. K. Walters and J. F. Davidson, 'The initial motion of a gas bubble formed in an inviscid liquid, Pt. 1: The two-dimensional bubble', *J. Fluid Mech.*, **12**, 408–417 (1962).
9. J. K. Walters and J. F. Davidson, 'The initial motion of a gas bubble formed in an inviscid liquid, Pt. 2: The three-dimensional bubble and the toroidal bubble', *J. Fluid Mech.*, **17**, 321–339 (1963).
10. R. M. Davies and G. I. Taylor, 'The mechanics of large bubbles rising through extended liquids and through liquids in tubes', *Proc. R. Soc. Ser. A*, **200**, 375–390 (1950).
11. J. T. Lindt, 'Note on the wake behind a two-dimensional bubble', *Chem. Eng. Sci.*, **26**, 1776–1777 (1971).
12. J. T. Lindt, 'On the periodic nature of the drag on a rising bubble', *Chem. Eng. Sci.*, **27**, 1775–1781 (1972).
13. J. R. Crabtree and J. Bridgewater, 'The wakes behind two-dimensional air bubbles', *Chem. Eng. Sci.*, **22**, 1517–1518 (1967).
14. R. Collins, 'Structure and behaviour of wakes behind two-dimensional air bubbles in water', *Chem. Eng. Sci.*, **20**, 851–883 (1965).
15. W. F. Bessler and H. Littman, 'Experimental studies of wakes behind circularly capped bubbles', *J. Fluid Mech.*, **185**, 137–151 (1987).
16. P. P. Wegener and J. Parlange, 'Spherical-cap bubbles', *Ann. Rev. Fluid Mech.*, **5**, 79–100 (1973).
17. L. Rosenhead, 'The formation of vortices from a surface of discontinuity', *Proc. R. Soc., Ser. A*, **134**, 170–192 (1931).
18. G. Tryggvason and H. Aref, 'Numerical experiments on Hele Shaw flow with a sharp interface', *J. Fluid Mech.*, **136**, 1–30 (1983).
19. S. H. Brecht and J. R. Ferrante, 'Vortex-in-cell simulations of buoyant bubbles in three dimensions', *Phys. Fluids*, **7**, 1166–1191 (1989).
20. J. C. S. Meng and J. A. L. Thomson, 'Numerical studies of some nonlinear hydrodynamic problems by discrete vortex element methods', *J. Fluid Mech.*, **84**, 433–453 (1978).

21. G. Ryskin and L. G. Leal, 'Numerical solution of free boundary problems in fluid mechanics. Part 1. The finite-difference technique', *J. Fluid Mech.*, **148,** 1–17 (1984).
22. G. Ryskin and L. G. Leal, 'Numerical solution of free boundary problems in fluid mechanics. Part 2. Buoyancy driven motion of a gas bubble through a quiescent liquid', *J. Fluid Mech.*, **148,** 19–35 (1984).
23. B. D. Nichols, C. W. Hirt and R. S. Hotchkiss, 'SOLA-VOF: a solution algorithm for transient fluid flow with multiple free boundaries', Los Alamos National Laboratories, *LA-8355*, 1980.
24. F. H. Harlow and J. E. Welch, 'Numerical calculation of time-dependent viscous incompressible flow of fluid with free surface', *Phys. Fluids*, **8,** 2182–2189 (1965).
25. R. D. Rowe and J. D. Bugg, 'A numerical study of large bubble dynamics', Proceedings of the Canadian Applied Mathematics Society Conference on Continuum Mechanics and its Applications, Hemisphere, Vancouver, 1988, pp. 611–620.
26. B. D. Nichols and C. W. Hirt, 'Numerical simulation of boiling water reactor vent-clearing hydrodynamics', *Nucl. Sci. Eng.*, **73,** 196–209 (1980).
27. L. A. Hageman and D. M. Young, *Applied Iterative Methods*, Academic Press, New York, 1981.
28. S. V. Patankar, *Numerical Heat Transfer and Fluid Flow*, Hemisphere, New York, 1980.
29. Control Data Corporation (CDC), *MAGEV: Mathematical and Geophysical Vector Library, Version 3.3*, 1984.
30. R. Collins, 'A simple model of the plane gas bubble in a finite liquid', *J. Fluid Mech.*, **22,** 763–771 (1965).